

Article

Fe,Ni-Based Metal–Organic Frameworks Embedded in Nanoporous Nitrogen-Doped Graphene as a Highly Efficient Electrocatalyst for the Oxygen Evolution Reaction

Panjuan Tang ^{1,†}, Biagio Di Vizio ^{1,†} , Jijin Yang ¹, Bhushan Patil ¹ , Mattia Cattelan ^{1,2,3,*} 
and Stefano Agnoli ^{1,2,3,*}

¹ Department of Chemical Sciences, University of Padova, Via F. Marzolo 1, 35131 Padova, Italy; panjuan.tang@phd.unipd.it (P.T.)

² National Interuniversity Consortium of Materials Science and Technology (INSTM), 50121 Florence, Italy

³ Consorzio Interuniversitario Reattività Chimica e Catalisi (CIRCC) Research Unit, University of Padova, 35131 Padova, Italy

* Correspondence: mattia.cattelan@unipd.it (M.C.); stefano.agnoli@unipd.it (S.A.); Tel.: +39-0498275845 (M.C.); +39-0498275167 (S.A.)

† These authors have equally contributed to this work.

Abstract: The quest for economically sustainable electrocatalysts to replace critical materials in anodes for the oxygen evolution reaction (OER) is a key goal in electrochemical conversion technologies, and, in this context, metal–organic frameworks (MOFs) offer great promise as alternative electroactive materials. In this study, a series of nanostructured electrocatalysts was successfully synthesized by growing tailored Ni-Fe-based MOFs on nitrogen-doped graphene, creating composite systems named MIL-NG-n. Their growth was tuned using a molecular modulator, revealing a non-trivial trend of the properties as a function of the modulator quantity. The most active material displayed an excellent OER performance characterized by a potential of 1.47 V (vs. RHE) to reach 10 mA cm⁻², a low Tafel slope (42 mV dec⁻¹), and a stability exceeding 18 h in 0.1 M KOH. This outstanding performance was attributed to the synergistic effect between the unique MOF architecture and N-doped graphene, enhancing the amount of active sites and the electron transfer. Compared to a simple mixture of MOFs and N-doped graphene or the deposition of Fe and Ni atoms on the N-doped graphene, these hybrid materials demonstrated a clearly superior OER performance.

Keywords: oxygen evolution reaction; electrocatalysts; metal–organic frameworks; N-doped graphene; hybrid materials



Citation: Tang, P.; Di Vizio, B.; Yang, J.; Patil, B.; Cattelan, M.; Agnoli, S. Fe,Ni-Based Metal–Organic Frameworks Embedded in Nanoporous Nitrogen-Doped Graphene as a Highly Efficient Electrocatalyst for the Oxygen Evolution Reaction. *Nanomaterials* **2024**, *14*, 751. <https://doi.org/10.3390/nano14090751>

Academic Editor: Raphaël Schneider

Received: 7 April 2024

Revised: 16 April 2024

Accepted: 23 April 2024

Published: 25 April 2024



Copyright: © 2024 by the authors. Licensee MDPI, Basel, Switzerland. This article is an open access article distributed under the terms and conditions of the Creative Commons Attribution (CC BY) license (<https://creativecommons.org/licenses/by/4.0/>).

1. Introduction

With the continuous growth of the world economy, fossil fuels such as oil, natural gas, and coal have been over-exploited as primary energy sources, causing serious environmental problems such as pollution and systematic negative impacts on the climate [1,2]. To overcome this, the development of a cleaner and sustainable energy infrastructure based on renewable sources and hydrogen as the primary energy vector is a promising route [3–5]. Thence, the demand for hydrogen and its exploitation in different sectors are increasing, and we need efficient methods for its large-scale production [6]. In this context, electrocatalytic water splitting is recognized as the most promising technology for producing sustainable hydrogen [7,8]. The development of catalysts with high activity [9,10] at low costs [11] for the oxygen evolution reaction (OER) is one of the most critical bottlenecks that still limits an important part of the electrolyser market [12]. Precious and critical metal oxides (such as RuO₂ and IrO₂) [13,14] have traditionally been used as electrocatalysts for the OER, however, their prohibitive cost prevents their large-scale production and commercial application. Transition-metal-based catalysts, such as oxides/hydroxides nanoparticles [15],

perovskite [16,17], and layered double hydroxides (LDHs) [18–20], are extremely promising given their good activity, large abundance, and good stability under alkaline conditions. Although transition-metal-based electrocatalysts display interesting performances, they still cannot compare with traditional noble-metal-based materials. Thence, doping and alloying have emerged as efficient methods for increasing the chemical activity, leading to the identification of mixed metal oxides/hydroxides materials (e.g., NiFeO_x [21,22] and Ni/Co/Fe layered double hydroxides [23,24]) as the most viable electrocatalysts for the OER.

On the other hand, metal–organic frameworks (MOFs), i.e., microporous crystalline materials made of metal nodes connected by organic building blocks, have been recently proposed as catalytic materials for energy conversion, given their large surface area, good thermal stability, high porosity, tunable functionalities, and large availability of open metal sites [25–29]. Materials Institute Lavoisier (MIL) compounds are a class of crystalline MOFs composed of different trivalent metal cations and carboxylic acid ligands [30–32]. Fe-, Ni-, and Co-based MOFs of the MIL family have been investigated as catalysts for the OER and extremely good results were obtained by the action of the redox chemistry of the metal nodes and tailoring the pore environment [33–35]. However, single-phase MOF materials suffer a very fundamental shortcoming for electrocatalysis, which is a poor electronic conductivity. Several literature works have reported solutions to this problem by supporting catalytically active MOFs on highly conductive and mechanically stable materials such as graphene oxide (GO) and nitrogen-doped graphene (NG) [36–38].

In recent years, GO [39] and NG [40] materials have captured a great deal of attention as applied materials owing to their affordable large-scale production and interesting properties, including large surface area, good electrical conductivity, and strong mechanical strength. The highly adaptable 2D structure of graphene and its easy chemical functionalization [41,42] provide a variety of active sites for its combination with other materials [43]. Therefore, the combination of graphene with MOFs represents an effective strategy for building high-performing nanocomposites that synergistically combine the best properties of the two moieties, as demonstrated by some works that have clearly proven the benefit in the incorporation of graphene to improve the electrocatalytic and photocatalytic properties of semiconducting MOFs [44–47].

Having in mind the OER in alkaline conditions as the target reaction, it is natural to study Fe-Ni-based compounds. Indeed, Ni-Fe-based oxides/oxyhydroxides have emerged as highly promising non-noble-metal-based electrocatalysts for the OER, with numerous studies showcasing the ability to modify their physicochemical properties by adjusting the stoichiometry of the Ni and Fe ions [48,49]. In particular, the effect of the incorporation of Fe ions into Ni catalysts can improve electron conductivity and reaction kinetics due to their optimal bond energetics for the adsorption of OER intermediates [50].

In this paper, hybrid nanoarchitectures with a tailored chemical composition and morphology, consisting of mixed metal MIL-126 supported on NG, were prepared through a solvothermal route by controlling the coordination reaction between Fe/Ni ions, biphenyl-4,4'-dicarboxylic acid (H₂bpdC), and NG. Particularly relevant is the “modulator approach” widely adopted in MOF synthesis, where a monocarboxylic acid is used to regulate the kinetics and morphology of the MOF growth [51,52]. In general, modulators facilitate the formation of metal clusters and slow down the crystal growth rate, thus avoiding the fast precipitation of amorphous products. Here, we used acetic acid (HOAc) as the modulator to control the nucleation density and growth rate of the MOF nanoparticles on the surface of NG to optimize the electrocatalytic activity of the resulting nanocomposite, noted as MIL-NG-n. The fabricated materials with different HOAc contents were extensively characterized, focusing on their structural and electrochemical behaviors. The evolution of the morphology, structure, and chemical composition of the MIL-NG-n along with variations in the acetic acid were investigated by powder X-ray diffraction (PXRD), scanning electron microscopy (SEM), energy-dispersive X-ray spectroscopy (EDX), transmission electron microscopy (TEM), X-ray photoemission spectroscopy (XPS), and the

Brunauer–Emmett–Teller (BET) method. The electrocatalytic behavior of the samples was tested in a three-electrode electrochemical cell using cyclic voltammetry (CV) and linear sweep voltammetry (LSV).

Importantly, the results indicated that the NG-MOF hybrids could promote the OER and induce higher electrocatalytic activity than the parent MOFs. When employed as an OER catalyst, the MIL-NG-3 had a low overpotential of 240 mV (at a current density of 10 mA cm⁻²) and low Tafel slope in alkaline solution, which outperforms most traditional crystalline inorganic materials.

2. Materials and Methods

2.1. Chemicals

All chemicals employed in this study were of analytical grade and were used without further purification. Biphenyl-4,4'-dicarboxylic acid (H₂bpdc), nickel(II) nitrate hexahydrate (Ni(NO₃)₂·6H₂O), iron(III) chloride hexahydrate (FeCl₃·6H₂O), potassium hydroxide (KOH), Nafion[®] 117 ~5% in ethanol and water, ethanol (CH₃CH₂OH, 99.7%), dimethylformamide (DMF), N-methyl-2-pyrrolidone (NMP), acetic acid (HOAc), fluorinated graphite, and ammonium hydroxide solution (28–30%) were provided by Merck & Co Inc., (Rahway, NJ, USA). Deionized water was supplied by a Millipore System.

2.2. Physical Chemical Characterizations

Powder X-ray diffraction (PXRD) patterns were recorded on a PANalytical PW3040/60 X'Pert PRO MPD (Malvern Panalytical B.V, Almelo, The Netherlands) X-ray diffractometer with Cu-Kα radiation (1.5418 Å). SEM images were obtained by a Zeiss Supra VP35 (Carl Zeiss SMT, Wetzlar, Germany) scanning electron microscope and an FEG-FIB Tescan Solaris with an EDX detector Ultim Max 65 (Oxford Instrument, Abingdon-on-Thames, UK). TEM images were obtained using an FEI Tecnai 12 operating under an accelerating voltage of 200 kV. The surface area and pore size characteristics of the synthesized samples were analyzed by N₂ adsorption and desorption measurements using an ASAP 2020 Micromeritics surface area and porosity analyzer (Norcross, GA, USA). Before the nitrogen adsorption/desorption measurements were performed, all samples were dried at 120 °C under vacuum for 12 h. Raman measurements were performed with a ThermoFisher DXR Raman microscope (Waltham, MA, USA) using a laser with an excitation wavelength of 780 nm (1 mW) and a 50× objective (Olympus, Tokyo, Japan). XPS spectra were acquired using the Mg Kα line (hν = 1253.6 eV) and a pass energy of 20 eV.

2.3. Electrochemical Measurements

OER tests were performed in a three-electrode cell with an Autolab potentiostat (Metrohm Group, Utrecht, The Netherlands), using a graphite counter electrode and an Ag/AgCl/saturated KCl reference electrode. The catalyst ink for the electrochemical analysis was prepared as follows: 4 mg of active powder was dispersed in H₂O (490 μL), DMF (490 μL), and a 5 wt % Nafion dispersion solution (20 μL), then sonicated for 1 h in an ultrasonic bath. After sonication, 8.5 μL of the mixture was drop cast on the glassy carbon electrode, which was previously polished with Al₂O₃ paste and rinsed with deionized water/ethanol. At the end of the procedure, a thin and mechanical robust catalyst layer with a loading of 0.2 mg cm⁻² and a fixed area of 0.159 cm² was obtained. Before the OER performance was tested, the catalysts were activated via CV scans at 100 mV s⁻¹ until they were stable. Linear sweep voltammetry was acquired by sweeping potentials from 0.93 to 1.9 V (vs. the Reversible Hydrogen Electrode (RHE)) with a forward scan rate of 5 mV s⁻¹ in 0.1 M KOH (pH 12.7). The current density was normalized to the geometrical surface area of the working electrode. All the polarization curves presented were corrected for the cell resistance. All the potentials reported in this study were referred against the RHE using Equation (1).

$$E(\text{RHE}) = E(\text{Ag}/\text{AgCl}) + (0.059 \times \text{pH}) + 0.183 \quad (1)$$

2.4. Synthesis of NG

A volume of 13 mL of degassed NMP was added to 120 mg of fluorinated graphite (FG) under a N_2 atmosphere, and the mixture was sonicated for 4 h. Then, NH_3 , produced by heating 200 mL of ammonium hydroxide solution at $60\text{ }^\circ\text{C}$ and dehydrating the resulting vapors with a KOH pad, was bubbled in the suspension kept at $0\text{ }^\circ\text{C}$ with an ice bath for 2 h. Finally, the mixture was transferred to a cold Teflon-lined autoclave and heated from room temperature to $140\text{ }^\circ\text{C}$ with a heating rate of $1\text{ }^\circ\text{C}/\text{min}$, where it was kept at the final temperature for 60 h. The Teflon-lined autoclave was then allowed to reach room temperature. After cooling down, the mixture was centrifuged and washed with DMF ($50\text{ mL} \times 2$), a mixture of DMF and water ($50\text{ mL} \times 2$), a mixture of MeOH and water ($50\text{ mL} \times 2$), MeOH ($50\text{ mL} \times 2$), and acetone ($50\text{ mL} \times 2$).

2.5. Synthesis of Bimetallic (Fe,Ni)-MIL-126

The (Fe,Ni)-MIL-126 was synthesized via a solvothermal route. H_2bpdc (22.4 mg) was dissolved in DMF (3 mL) under ultrasonication, while $FeCl_3 \cdot 6H_2O$ (27 mg) and $Ni(NO_3)_2 \cdot 6H_2O$ (46.6 mg) were dissolved in 6 mL of DMF and 300 μL of CH_3COOH (5 mmol). The solution was poured into a Teflon-lined autoclave and heated to $150\text{ }^\circ\text{C}$ with a heating rate of $5\text{ }^\circ\text{C}$ per min, where it was maintained at this temperature for 15 h. After cooling down to room temperature, the mixture was centrifuged and washed with DMF and MeOH multiple times.

2.6. Synthesis of MIL-NG-n Hybrid

The schematics of the synthesis of the MIL-NG-n hybrids are reported in Figure 1. To prepare the MIL-NG-n hybrids, an amount of 5 mg of NG was added to 9 mL of DMF and then kept at room temperature for 1 h until a homogeneous suspension was obtained. Then, $FeCl_3 \cdot 6H_2O$ (27 mg) and $Ni(NO_3)_2 \cdot 6H_2O$ (46.6 mg) were added, and the suspension was further sonicated for 1 h and then stirred for 12 h. Afterward, different quantities of CH_3COOH (HOAc) (see Table 1) and H_2bpdc (22.4 mg) were added to the mixture. After sonicating the solution for 1 h, the reaction vessel was sealed and heated up to $150\text{ }^\circ\text{C}$ with a heating rate of $5\text{ }^\circ\text{C}/\text{min}$, where it was kept at the final temperature for 15 h. After cooling down, the mixture was centrifuged and washed with DMF ($50\text{ mL} \times 3$) and MeOH ($50\text{ mL} \times 3$).

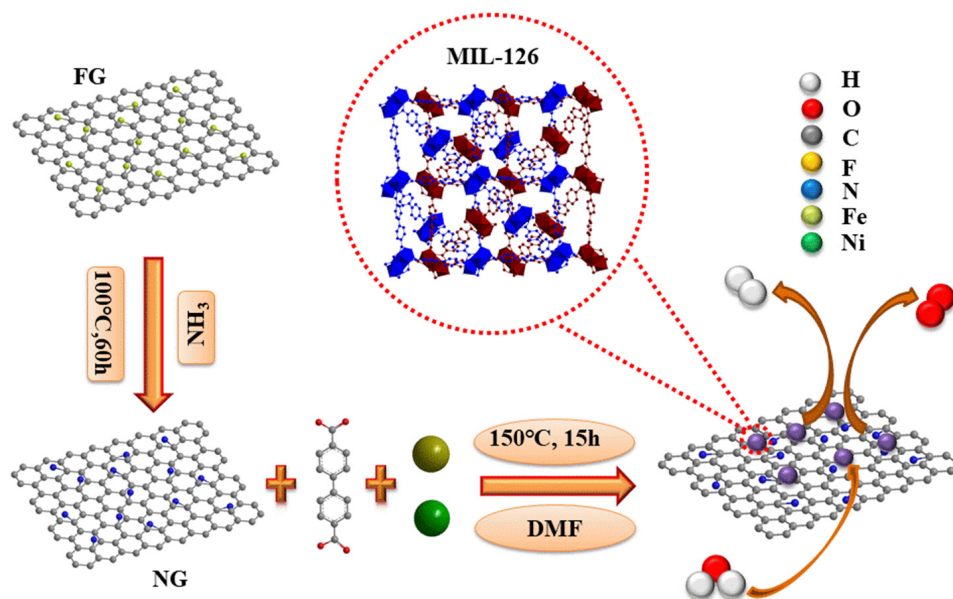


Figure 1. Schematic illustration of the synthesis of MIL-NG-n hybrids.

Table 1. HOAc quantity used in the synthesis of the different nanocomposites. Other conditions are: 5 mg NG; 0.10 mmol FeCl₃·6H₂O; 0.16 mmol NiCl₂·6H₂O; 0.10 mmol H₂bpdC; 9 mL of DMF.

	MIL-NG-1	MIL-NG-2	MIL-NG-3	MIL-NG-4	MIL-NG-5	MIL-NG-6
HOAc (mmol)	/	0.5	1	1.5	2	3

2.7. Synthesis of Bimetallic (Fe,Ni)-NG

To synthesize the (Fe,Ni)-NG hybrid, an amount of 5 mg of NG was added to 9 mL of DMF. Then, the mixture was sonicated at room temperature for 1 h until a homogeneous suspension was obtained. Then, FeCl₃·6H₂O (27 mg) and Ni(NO₃)₂·6H₂O (46.6 mg) were added to the mixture, sonicated for 1 h, and stirred for 12 h. Then, the reaction vessel was sealed and heated up to 150 °C with a heating rate of 5 °C/min, where it was kept at the final temperature for 15 h. After cooling down, the mixture was centrifuged and washed with DMF and MeOH multiple times.

2.8. Synthesis of (Fe,Ni)-MIL-126-NG-mix

To prepare the (Fe,Ni)-MIL-126-NG-mix, i.e., the physical mixture of the NG and the MOF, 2 mg of NG and 2 mg of (Fe,Ni)-MIL-126 were mixed by extensive grinding in an agate mortar.

3. Results and Discussion

The formation process of the MIL-NG-n hybrids is illustrated in Figure 1, while Table 1 reports the different amounts of modulator (HOAc) used in the synthesis, which was tuned from 0 to 3 mol. The in situ growth of MOFs on functionalized graphene is one of the most extensively used strategies for MOF/graphene hybrids [31,45]. This method ensures the uniform growth of MOFs on graphene, fostering a strong interaction between the two materials. This interaction arises from the abundant functional group of NG, and N is about 20% of the C, which can coordinate metal ions during the synthesis and facilitate the in situ nucleation and growth of MOF nanocrystals. In this paper, we specifically used NG deriving from fluorinated graphite, because this special synthesis route allows for achieving a very high level of nitrogen doping, with pyridinic and pyrrolic groups in an approximated ratio of 2:1 (see Supporting Information, Figures S1 and S2).

The crystallographic structures of the as-prepared (Fe,Ni)-MIL-126 and the MIL-NG-n nanocomposites were examined by PXRD (Figure 2a). The (Fe,Ni)-MIL-126 nanocomposite showed a diffraction pattern compatible with the two-fold interpenetrated structure based on Fe³⁺ ions and bpdC linkers reported by Serre et al. in 2012 (MIL-126(Fe), CCDC code MIBMER) [30]. The well-defined diffraction peaks confirm the high crystallinity of (Fe,Ni)-MIL-126 [31]. The MIL-NG-3, MIL-NG-4, MIL-NG-5, and MIL-NG-6 nanocomposites showed similar diffraction peaks as (Fe,Ni)-MIL-126, suggesting that the crystallinity of (Fe,Ni)-MIL-126 was not disrupted by the interaction with NG, i.e., the links between the organic bridges and metal ions were not interrupted.

However, comparing the XRD pattern of (Fe,Ni)-MIL-126 with those of MIL-NG-1 and MIL-NG-2, the characteristic diffraction peaks are much broader, indicating a lower crystallinity of the materials. Probably, in this case, the low concentration of modulator produces a non-uniform crystal growth allowing for late nucleation events [53]. Moreover, it has been reported that, in the absence of a modulator, a poorly crystalline MIL-88D phase can be obtained as well [54]. On the other hand, with the increase in HOAc from 1 mmol to 3 mmol, the characteristic peaks of the target MOF became well-defined, indicating that a minimum quantity of modulator is necessary to promote crystallization. Nonetheless, there was a marked decrease in the MOF yield indirectly visible by a reduction in the PXRD intensity. These findings are consistent with results reported by Forgan et al., who demonstrated that coordination modulation typically slows down the kinetics, allowing

the formation of the most stable thermodynamic compounds to be reached (i.e., two-fold interpenetrated MIL-126) [54].

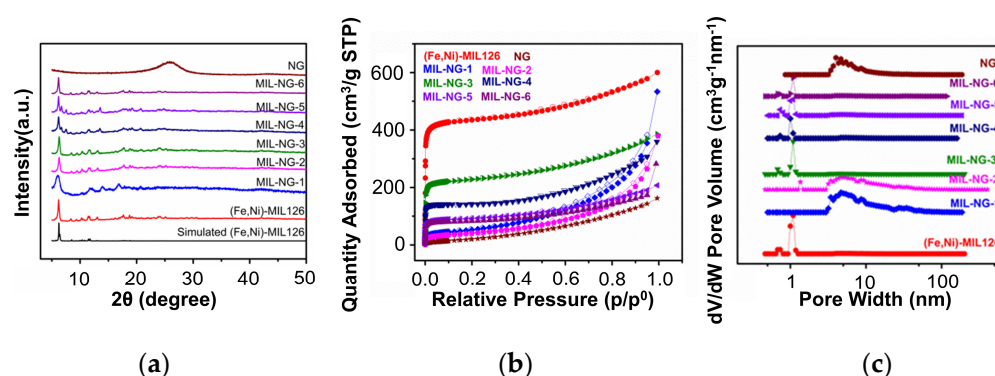


Figure 2. (a) XRD, (b) BET, and (c) pore size distribution patterns of as-prepared NG-MIL-n, (Fe,Ni)-MIL-126 and NG samples.

The porous features and BET specific surface areas of (Fe,Ni)-MIL-126, NG, and all the MIL-NG-n hybrids were investigated by nitrogen isothermal adsorption/desorption measurements at 77 K. The BET analysis results are reported in Table 2. Figure 2b shows that the (Fe,Ni)-MIL-126, MIL-NG-3, MIL-NG-4, MIL-NG-5, and MIL-NG-6 hybrid samples exhibited a typical type I isotherm, confirming that all the composites were predominantly microporous materials, whereas the NG, MIL-NG-1, and MIL-NG-2 hybrids presented a typical type IV adsorption isotherm shape with a hysteresis loop, demonstrating the existence of mesoporous characteristics. Compared with the MIL-NG-n hybrid, the pure (Fe,Ni)-MIL-126 had much better N₂ adsorption capacity, particularly below a pressure of $P/P_0 = 0.1$. The increase in the quantity of HOAc induced a non-monotonic trend of the surface area: for low or no quantity, i.e., from MIL-NG-1 to MIL-NG-3, there was a clear increase in porosity, whereas a significant decrease was observed at higher concentration. A similar trend is discussed above for the XRD data, with an increase in crystallinity from MIL-NG-1 to MIL-NG-3 followed by a decrease in the MOF yield from MIL-NG-3 to MIL-NG-6. The pore volumes and pore size distributions from the N₂ isotherms were obtained by using a nonlinear density functional theory model. The pores size in (Fe,Ni)-MIL-126, MIL-NG-3, MIL-NG-4, MIL-NG-5, and MIL-NG-6 were mainly centered at 1 nm, indicating the presence of micropores, consistent with the N₂ adsorption isotherm in Figure 2c. The MIL-NG-1, MIL-NG-2, and NG also showed some mesoporosity, with most of the pore sizes in the 5 nm range.

Table 2. BET method data.

Sample	Type of Porosity	Specific Surface Area (m ² /g)	Pore Size (nm)
NG	IV type and hysteresis loop, mesoporous	92	5
(Fe,Ni)-MIL-126	I type, microporous	1720	1
MIL-NG-1	IV type and hysteresis loop, mesoporous	148	5
MIL-NG-2	IV type and hysteresis loop, mesoporous	196	5
MIL-NG-3	I type, microporous	884	1
MIL-NG-4	I type, microporous	595	1
MIL-NG-5	I type, microporous	352	1
MIL-NG-6	I type, microporous	285	1

Among all the MIL-NG-*n* hybrids, MIL-NG-3 exhibited a much higher surface area, which is a favorable aspect for electrocatalysis, given the larger exposure of catalytic active sites and improved resulting mass transport.

To visualize how the (Fe,Ni)-MIL-126 and NG components were assembled into the hybrid materials, we performed SEM and TEM measurements. The SEM images of the NG-MIL-*n* samples are reported in Figures S3 and S4 along with EDX mapping and spectra. The EDX analysis proves the co-presence NG and MOF in the same position detectable from N and C signals, mainly related to NG, and Fe and Ni absorption peaks, associated with the MOF [52]. The structures of the MIL-NG-*n* samples prepared with different amounts of modulator are shown in Figure 3a–f, where it can be clearly seen that (Fe,Ni)-MIL-126 nanoparticles, in a range from 50 to 200 nm, are dispersed quite homogeneously on NG flakes. However, as the content of HOAc changes, the morphology of the resulting MOF shows no clear changes at these magnifications. In Figure S5, the TEM image of the bare NG supports is reported for comparison.

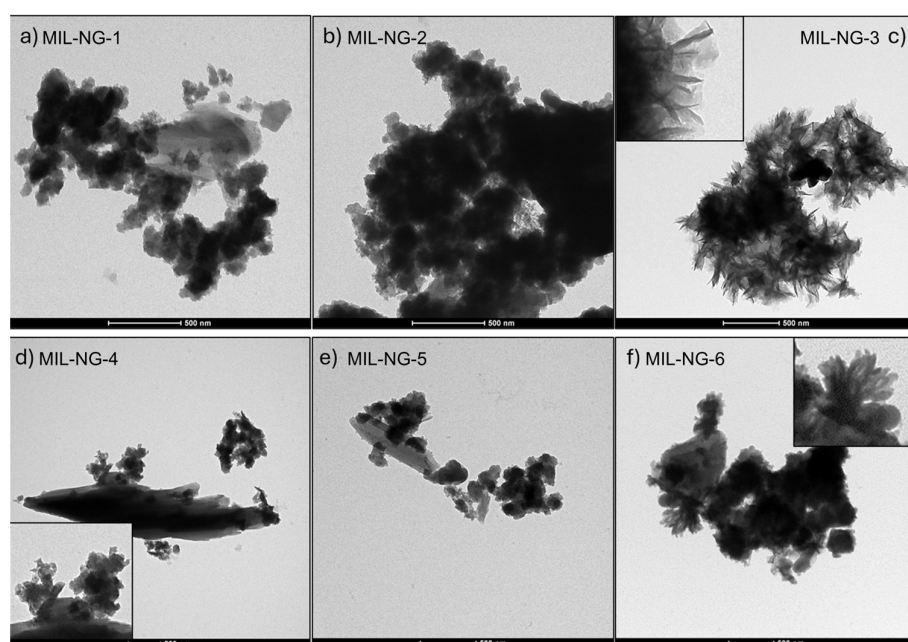


Figure 3. TEM images of as-prepared (a) MIL-NG-1, (b) MIL-NG-2, (c) MIL-NG-3, (d) MIL-NG-4, (e) MIL-NG-5, and (f) MIL-NG-6, scale bars 500 nm.

The materials' characterization demonstrates that the obtained MIL-NG-*n* hybrids possessed the necessary characteristics for a highly efficient OER electrocatalyst with a highly dispersed ensemble of exposed metal centers, i.e., (Fe,Ni)-MIL-126, in close contact with a highly conductive material, i.e., NG, for fast electron transfer.

To prove that the hybrid materials had superior electrocatalytic activity, firstly, we compared the bare carbon support, the pure (Fe,Ni)-MIL-126, the physical mixture of NG and (Fe,Ni)-MIL-126 ((Fe,Ni)-MIL-126-NG-mix), and a composite produced by the direct metalation of the nitrogen centers of NG with Ni and Fe metal cations ((Fe,Ni)-NG). As reported in Figure 4a the NG, bimetallic (Fe,Ni)-NG, and (Fe,Ni)-MIL-126-NG-mix showed low OER activity, whereas for (Fe,Ni)-MIL-126, the electroactivity started to become significant. This indicates that the metal centers are obviously essential for catalysis, however, to achieve a good performance, it is also necessary to guarantee that they are efficiently utilized, i.e., directly exposed to the electrolyte. The other important point for high electrochemical activity is also the ability to transfer electrons, which is possible only if the MOF, which is rather electrically resistive and is efficiently connected to a highly conductive support. Indeed, any MIL-NG-*n* hybrid electrocatalyst (Figure 4b)

showed much higher activity than all the samples reported in Figure 4a, demonstrating the synergistic effects of NG and (Fe,Ni)-MIL-126.

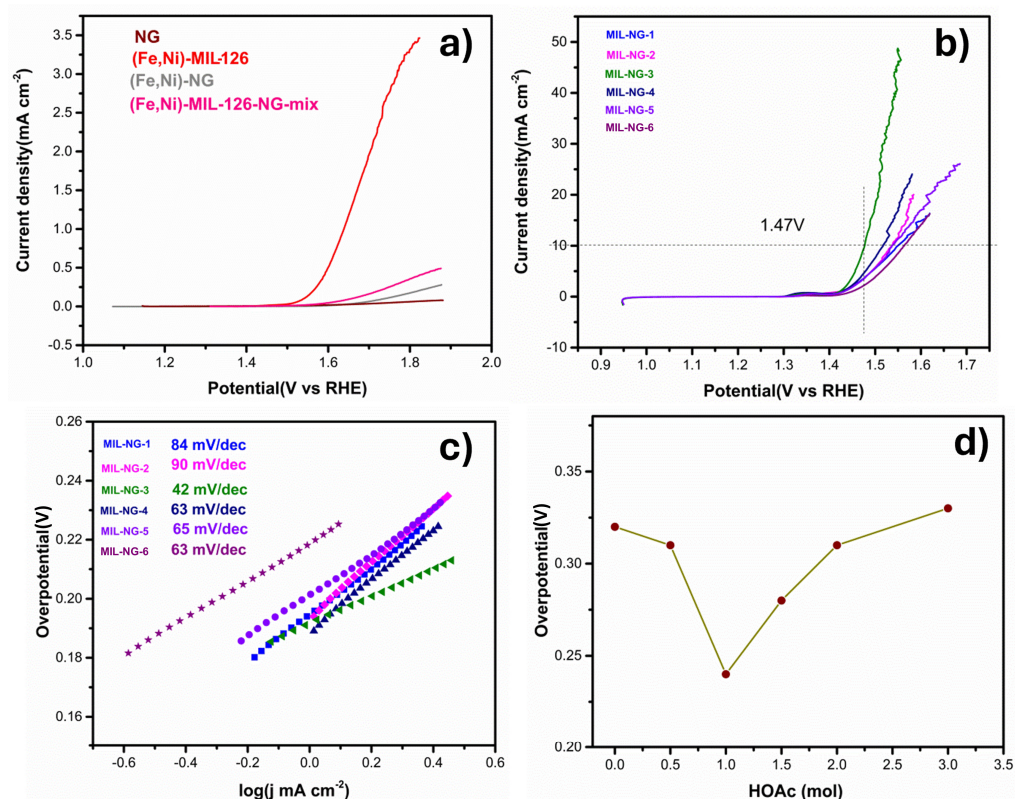


Figure 4. OER current densities of glassy carbon (GC)-supported in 0.1 M KOH at 5 mV s⁻¹: (a) LSV curves of NG, (Fe,Ni)-MIL-126, bimetallic (Fe,Ni)-NG, and (Fe,Ni)-MIL-126-NG-mix, (b) LSV curves of MIL-NG-n, (c) Tafel plots of MIL-NG-n, and (d) the overpotential as a function of the molar of HOAc.

In Figure 4a, when comparing the performances of pure (Fe,Ni)-MIL-126 and the physically mixed composite 50% in weight with NG ((Fe,Ni)-MIL-126-NG-mix), it seems that the OER performance was hindered by the NG when the two components were simply mixed. Specifically, the current density at 1.9 V vs. RHE of the (Fe,Ni)-MIL-126-NG-mix was about seven times lower than that of the pure MOF. This suggests that NG may have covered some metallic centers of the MOF, or in any case, it did not significantly help the activity of the MOF, as it was not electrically connected to it. These observations underscore the critical importance of the synthesis approach proposed in our work [45,55], which facilitates an intimate contact between MOF and graphenic materials. Hybrid materials are not achievable through simple mixing or metal doping, and only when effectively formed do they have enhanced conductivity and a significantly increased active surface area.

To understand the modulator effect, the overpotential necessary to reach 10 mA cm⁻² for different hybrids was plotted in Figure 4d. MIL-NG-3 was the best-performing electrode with an overpotential of 240 mV, which was significantly lower compared to the other non-hybrid electrodes in Figure 4a, which did not even reach 10 mA cm⁻² at an overpotential of 670 mV. Moreover, at an overpotential of 310 mV, the current densities of MIL-NG-3 could reach 40 mA cm⁻², which was 2.6 and 4 times more than MIL-NG-4 and MIL-NG-5, respectively.

Furthermore, different concentrations of HOAc exhibited a discernible pattern in terms of catalytic activity, reaching a peak value at 1 mol of HOAc (MIL-NG-3). Similar trends were observed in PXRD, with well-defined MOF peaks at the critical minimum modulator quantity for MIL-NG-3 (refer to Table 1), and in BET, showing the larger surface area of the

hybrids for MIL-NG-3 (refer to Table 2). The above results indicate that HOAc can favor high OER activity for an increase in MOF crystallinity, and a critical quantity of modulator is necessary to have a diffuse nucleation and controlled crystal growth.

The OER kinetics were analyzed by Tafel plots, as shown in Figure 4c. A low value of the Tafel slope is highly advantageous, as it allows for the achievement of a high catalytic current density at low applied potentials. The obtained Tafel slopes are summarized in Table 3. The results demonstrate that MIL-NG-3 exhibited rapid kinetics for OER compared to other MIL-NG-n hybrids, further explaining the enhancement of OER properties. Our best catalyst resulted in being one of the best-performing MOF–graphene hybrids in the literature, see Table 4.

To better investigate the enhancement of OER activity for NG-MIL-3, electrochemically active areas (ECSA) can be evaluated from the electrochemical double-layer capacitance (C_{dl}) by conducting variable scan rate CV in the non-Faradaic region, see Figure 5a and Table 3. MIL-NG-3 had the highest C_{dl} value and the best OER performance, suggesting that its higher activity was linked to the more electrochemically available active sites at the solid–liquid interface, which was also linked to the higher surface area detectable by BET, see Table 2. The principal electrochemical key parameters of MIL-NG-n are summarized in Table 3.

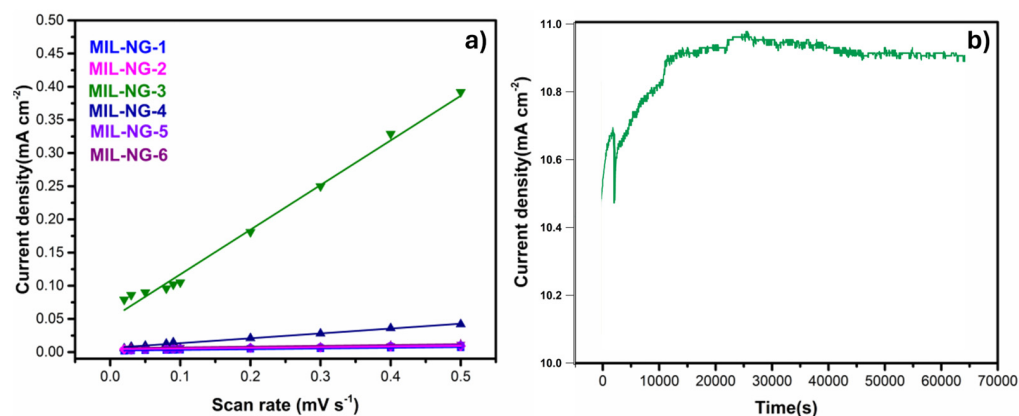


Figure 5. (a) Plot of current density vs. scan rate. (b) Chronoamperometric responses of NG-MIL-3 catalysts obtained at 1.47 V (vs. RHE) in 0.1 M KOH solution.

Stability is also an important parameter for evaluating the properties of an electrocatalyst. In Figure 5b, the long-term durability of MIL-NG-3 is reported. A test was performed using current-time chronoamperometry at a constant voltage of 1.47 V (vs. RHE) in 0.1 M KOH. The obtained current density increased slightly in the first 4 h, rising from 10.4 to about 10.9 mA cm⁻², and then remained quite constant for the following 13.5 h, indicating a great overall stability.

The PXRD investigation of the materials after the electrochemical was inconclusive, showing a substantial amorphization but without the identification of new ordered phase, so Raman spectroscopy was employed to understand the effect of the OER on the catalyst. The Raman signatures of NG, (Fe,Ni)-MIL126, and MIL-NG-n are shown in Figure 6. For NG, the two peaks are ascribed to the characteristic D-band and G-band of carbonaceous materials [56]. The Raman spectra of the MIL-NG-n hybrid materials show no significant differences compared with (Fe,Ni)-MIL-126. The MIL-NG-3 Raman spectra after 18 h chronoamperometry in the OER show peaks indicative of Ni(OH)₂ phases [57]. This suggests a potential transformation of the materials, likely occurring within the first 4 h, coinciding with the visible increase in OER performance, see Figure 4b. An XPS analysis post-chronoamperometry in Figure S6 confirms the presence of Ni(OH)₂/NiOOH and FeOOH. The notable activity and stability in the OER can, therefore, be ascribed to the existence of these materials; indeed, it is well-established that they are among the most used and stable materials for the OER in an alkaline medium [24,58].

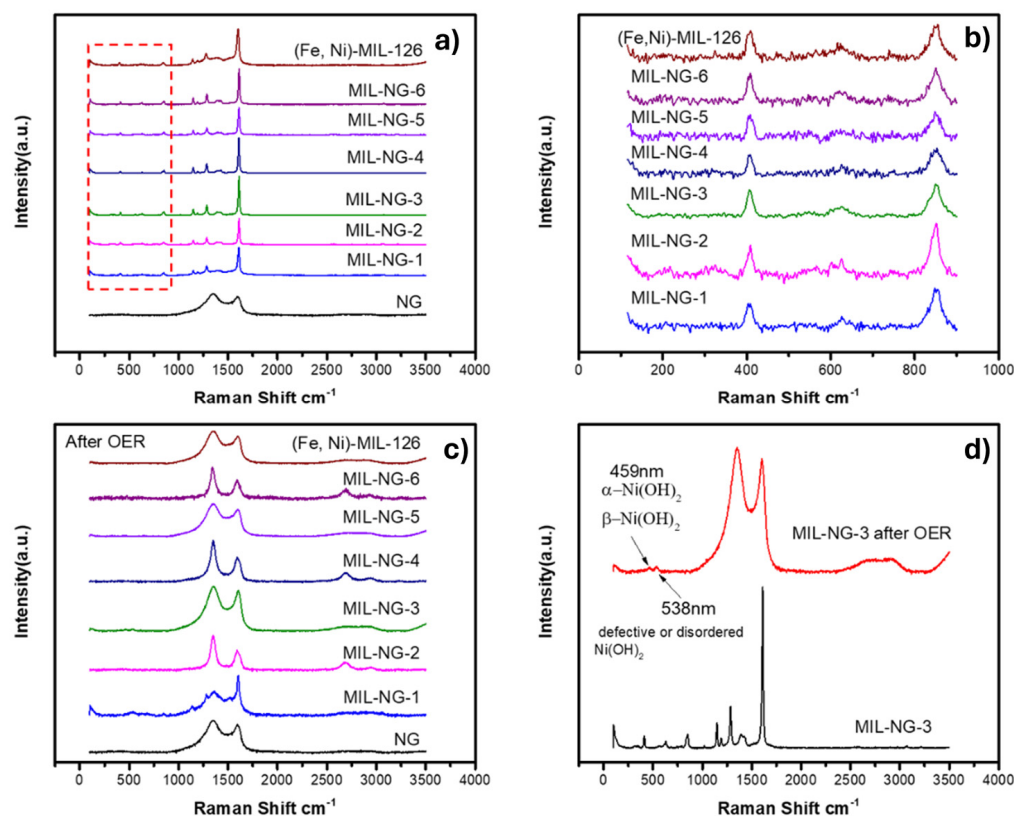


Figure 6. Raman spectra of the prepared (a) MIL-NG-*n*, (Fe,Ni)-MIL-126, and NG fresh samples, (b) detailed spectra from 100 to 900 cm^{-1} in (a), (c) MIL-NG-*n*, (Fe,Ni)-MIL-126, and NG after OER samples, and (d) comparison of MIL-NG-3 before and chronoamperometry in OER.

Indeed, the limited stability of MOFs in strongly alkaline solutions and their restructuring in metal oxo-hydroxide have eventually emerged in the literature [59], but this apparent problem can also offer new synthetic strategies, as demonstrated in a recent seminal paper [60], where extremely active OER catalysts were obtained by sandwiching metal hydroxide nanosheets in between organic layers of pi-staked organic linkers, forming a so called metal hydroxide–organic framework. We can hypothesize that this is what happened in our materials, although in a less ordered and controlled way: the metal nodes rearranged into mixed metal oxo-hydroxide that remained confined within an organic shell made by the organic linker and the NG.

Finally, it should be highlighted that our synthesis protocol is simple, safe, cost-effective, and leads to catalysts with excellent activity. Therefore, with further durability studies, they can be considered for application in the development of real electrolyzers.

Table 3. Summary of electrochemical OER performance data of MIL-NG-*n*.

Sample	Tafel Slope/ mV dec^{-1}	Overpotential at $10 \text{ mA cm}^{-2}/\text{mV}$	Cdl/ mF cm^{-2}
MIL-NG-1	84	320	0.01
MIL-NG-2	90	310	0.009
MIL-NG-3	42	240	0.67
MIL-NG-4	63	280	0.07
MIL-NG-5	65	310	0.012
MIL-NG-6	63	330	0.015

Table 4. Comparison of OER performances of Ni-Fe based materials and MOF-graphene composites.

Components	E_{OER} (V) at 10 mA cm^{-2}	Tafel $\text{mV}\cdot\text{dec}^{-1}$	Refs.
MIL-NG-3	1.47	42	/
MIL-126(FeNi)-700	2.0		[61]
Fe ₁ Ni ₂ -BDC	1.49	35	[26]
Fe/Ni/Co(Mn)-MIL-53/NF	1.45	53.5	[35]
Fe ²⁺ -NiFe LDH	1.479	40.4	[62]
NiFeV LDHs	1.422	42	[63]
NiFe LDHs Nanosheets	1.459	62.9	[64]
flame-engraved NiFe-LDH	1.48	69	[65]
Fe–Ni–P/rGO-400	1.47	63	[66]
Ni ₂ P@C/GO (NiBTC)	1.515	44	[67]
NGO/Ni7S6 (Ni-MOF-74)	1.61	45	[68]
Ni-NiO/N-rGO	1.47	43	[28]
Ni-MOF-600	1.6	66	[69]
CoP/rGO-400 (ZIF 67)	1.57	66	[70]

4. Conclusions

We synthesized a series of highly active Ni,Fe-based MOFs within NG using meticulous NG-templated MOF growth with a ‘modulator’ approach. The resulting hybrids, called MIL-NG-n, exhibited an exceptional OER performance, with their physical–chemical properties showing a complex trend with respect to the modulator quantify. The outstanding OER performance was attributed to synergistic effects of the MOF’s large surface area and NG conductivity, enhancing the electrocatalytic activity, electrical conductivity, mass transfer, and overall activity. Among the synthesized catalysts, MIL-NG-3 was the most efficient, with an exceptional 240 mV overpotential to reach 10 mA cm^{-2} and a low Tafel slope of 42 mV dec^{-1} . This work shows a significant advancement in the field, serving as a valuable reference for preparing electrocatalysts for OER applications without the use of critical raw materials. This approach opens up new avenues for preparing sustainable and high-performance electrocatalysts, contributing to green energy technologies.

Supplementary Materials: The following supporting information can be downloaded at: <https://www.mdpi.com/article/10.3390/nano14090751/s1>, Figure S1: NG Fourier Transformed Infrared (FT-IR), prepared on KBr disk. Spectrum recorded with a Nicolet Nexus FT-IR spectrometer. The characteristic NG bands of C–N ($\sim 1160 \text{ cm}^{-1}$) and C=C ($\sim 1550 \text{ cm}^{-1}$) vibrations are visible.; Figure S2: NG not-monochromatic X-ray photoemission spectroscopy (XPS) lines of C1s and N1s, deconvoluted into single chemically shifted components. Figure S3: SEM images of as-prepared (a) MIL-NG-1, (b) MIL-NG-2, (c) MIL-NG-3, (d) MIL-NG-4, (e) MIL-NG-5, (f) MIL-NG-6. Figure S4: SEM EDX mapping of MIL-NG-3 and EDX spectrum. Figure S5: TEM image of NG, scale bar 100 nm. Figure S6: Ni 2p_{3/2} and Fe 2p XPS lines of MIL-NG-3 after chronoamperometry in OER indicating the presence of Ni(OH)₂/NiOOH and FeOOH.

Author Contributions: Conceptualization, S.A. and M.C.; methodology, B.P.; validation, M.C., P.T., J.Y. and B.D.V. formal analysis investigation; data curation, M.C.; writing—original draft preparation, P.T., S.A. and M.C.; writing—review and editing, M.C.; supervision, S.A.; funding acquisition, S.A. All authors have read and agreed to the published version of the manuscript.

Funding: This research was funded by the University of Padova, through the project P-DiSC #01BIRD2022-UNIPD by the Italian Ministry of University and Research (MUR) through the grant PRIN 2022 2022E5L4Y2. We acknowledge financial support under the National Recovery and Resilience Plan (NRRP), Mission 4, Component 2, Investment 1.1, by the MUR, funded by the European Union—NextGenerationEU—Project Title “Microscopic approach to Understand Synergies in Electrocatalysis”—Project No. 2022E5L4Y2 (CUP: C53D23003780006). We acknowledge support from Project C2 chemical complexity (CUP: C93C22009260001) under the MUR program “Dipartimenti di Eccellenza 2023–2027.

Data Availability Statement: Data are contained within the article.

Acknowledgments: P.T. and J.Y. acknowledge the China scholarship council for the financial support No. 201707565021 and No. 202006880005, respectively. MC acknowledges a research contract on Green Topics from action IV.6 of the PON Research and Innovation 2014–2020 “Education and research for recovery—REACT-EU” program. contract 19-G-12549-1. The authors acknowledge Dr. Jacopo Nava for assistance during the SEM-EDX acquisitions.

Conflicts of Interest: The authors declare no conflicts of interest.

References

1. Turner, J.A. A Realizable Renewable Energy Future. *Science* **1999**, *285*, 687–689. [[CrossRef](#)] [[PubMed](#)]
2. Lunardon, M.; Kosmala, T.; Durante, C.; Agnoli, S.; Granozzi, G. Atom-by-Atom Identification of Catalytic Active Sites in Operando Conditions by Quantitative Noise Detection. *Joule* **2022**, *6*, 617–635. [[CrossRef](#)]
3. Capurso, T.; Stefanizzi, M.; Torresi, M.; Camporeale, S.M. Perspective of the Role of Hydrogen in the 21st Century Energy Transition. *Energy Convers. Manag.* **2022**, *251*, 114898. [[CrossRef](#)]
4. Kosmala, T.; Baby, A.; Lunardon, M.; Perilli, D.; Liu, H.; Durante, C.; Di Valentin, C.; Agnoli, S.; Granozzi, G. Operando Visualization of the Hydrogen Evolution Reaction with Atomic-Scale Precision at Different Metal–Graphene Interfaces. *Nat. Catal.* **2021**, *4*, 850–859. [[CrossRef](#)]
5. Lunardon, M.; Cattelan, M.; Agnoli, S.; Granozzi, G. Toward Sustainable and Effective HER Electrocatalysts: Strategies for the Basal Plane Site Activation of Transition Metal Dichalcogenides. *Curr. Opin. Electrochem.* **2022**, *34*, 101025. [[CrossRef](#)]
6. Guan, D.; Wang, B.; Zhang, J.; Shi, R.; Jiao, K.; Li, L.; Wang, Y.; Xie, B.; Zhang, Q.; Yu, J.; et al. Hydrogen Society: From Present to Future. *Energy Environ. Sci.* **2023**, *16*, 4926–4943. [[CrossRef](#)]
7. Lee, J.E.; Jeon, K.-J.; Show, P.L.; Lee, I.H.; Jung, S.-C.; Choi, Y.J.; Rhee, G.H.; Lin, K.-Y.A.; Park, Y.-K. Mini Review on H₂ Production from Electrochemical Water Splitting According to Special Nanostructured Morphology of Electrocatalysts. *Fuel* **2022**, *308*, 122048. [[CrossRef](#)]
8. Lv, X.-W.; Tian, W.-W.; Yuan, Z.-Y. Recent Advances in High-Efficiency Electrocatalytic Water Splitting Systems. *Electrochem. Energy Rev.* **2023**, *6*, 23. [[CrossRef](#)]
9. Zhu, Y.P.; Guo, C.; Zheng, Y.; Qiao, S.-Z. Surface and Interface Engineering of Noble-Metal-Free Electrocatalysts for Efficient Energy Conversion Processes. *Acc. Chem. Res.* **2017**, *50*, 915–923. [[CrossRef](#)]
10. Zhang, W.; Lai, W.; Cao, R. Energy-Related Small Molecule Activation Reactions: Oxygen Reduction and Hydrogen and Oxygen Evolution Reactions Catalyzed by Porphyrin- and Corrole-Based Systems. *Chem. Rev.* **2016**, *117*, 3717–3797. [[CrossRef](#)]
11. Wu, G.; Zelenay, P. Nanostructured Nonprecious Metal Catalysts for Oxygen Reduction Reaction. *Acc. Chem. Res.* **2013**, *46*, 1878–1889. [[CrossRef](#)] [[PubMed](#)]
12. Lunardon, M.; Kosmala, T.; Ghorbani-Asl, M.; Krasheninnikov, A.V.; Kolekar, S.; Durante, C.; Batzill, M.; Agnoli, S.; Granozzi, G. Catalytic Activity of Defect-Engineered Transition Metal Dichalcogenides Mapped with Atomic-Scale Precision by Electrochemical Scanning Tunneling Microscopy. *ACS Energy Lett.* **2023**, *8*, 972–980. [[CrossRef](#)] [[PubMed](#)]
13. Hess, F. Corrosion Mechanism and Stabilization Strategies for RuO₂ and IrO₂ Catalysts in the Electrochemical Oxygen Evolution Reaction. *Curr. Opin. Electrochem.* **2023**, *41*, 101349. [[CrossRef](#)]
14. Li, G.; Li, S.; Ge, J.; Liu, C.; Xing, W. Discontinuously Covered IrO₂–RuO₂@Ru Electrocatalysts for the Oxygen Evolution Reaction: How High Activity and Long-Term Durability can Be Simultaneously Realized in the Synergistic and Hybrid Nano-Structure. *J. Mater. Chem. A* **2017**, *5*, 17221–17229. [[CrossRef](#)]
15. Li, X.-P.; Huang, C.; Han, W.-K.; Ouyang, T.; Liu, Z.-Q. Transition Metal-Based Electrocatalysts for Overall Water Splitting. *Chin. Chem. Lett.* **2021**, *32*, 2597–2616. [[CrossRef](#)]
16. Tang, J.; Xu, X.; Tang, T.; Zhong, Y.; Shao, Z. Perovskite-Based Electrocatalysts for Cost-Effective Ultrahigh-Current-Density Water Splitting in Anion Exchange Membrane Electrolyzer Cell. *Small Methods* **2022**, *6*, e2201099. [[CrossRef](#)]
17. Abdelghafar, F.; Xu, X.; Jiang, S.P.; Shao, Z. Perovskite for Electrocatalytic Oxygen Evolution at Elevated Temperatures. *ChemSusChem* **2024**, *4*, e202301534. [[CrossRef](#)]
18. Cai, Z.; Bu, X.; Wang, P.; Ho, J.C.; Yang, J.; Wang, X. Recent Advances in Layered Double Hydroxide Electrocatalysts for the Oxygen Evolution Reaction. *J. Mater. Chem. A* **2019**, *7*, 5069–5089. [[CrossRef](#)]
19. Yang, L.; Liu, Z.; Zhu, S.; Feng, L.; Xing, W. Ni-Based Layered Double Hydroxide Catalysts for Oxygen Evolution Reaction. *Mater. Today Phys.* **2021**, *16*, 100292. [[CrossRef](#)]
20. Wang, Y.; Yan, D.; El Hankari, S.; Zou, Y.; Wang, S. Recent Progress on Layered Double Hydroxides and Their Derivatives for Electrocatalytic Water Splitting. *Adv. Sci.* **2018**, *5*, 1800064. [[CrossRef](#)]
21. Yang, H.; Liu, Y.; Luo, S.; Zhao, Z.; Wang, X.; Luo, Y.; Wang, Z.; Jin, J.; Ma, J. Lateral-Size-Mediated Efficient Oxygen Evolution Reaction: Insights into the Atomically Thin Quantum Dot Structure of NiFe₂O₄. *ACS Catal.* **2017**, *7*, 5557–5567. [[CrossRef](#)]
22. Qiu, Y.; Xin, L.; Li, W. Electrocatalytic Oxygen Evolution over Supported Small Amorphous Ni–Fe Nanoparticles in Alkaline Electrolyte. *Langmuir* **2014**, *30*, 7893–7901. [[CrossRef](#)] [[PubMed](#)]
23. Xu, X.; Yu, X.; Guo, K.; Dong, L.; Miao, X. Alkaline Media Regulated NiFe-LDH-Based Nickel–Iron Phosphides toward Robust Overall Water Splitting. *Catalysts* **2023**, *13*, 198. [[CrossRef](#)]

24. Salvò, D.; Mosconi, D.; Neyman, A.; Bar-Sadan, M.; Calvillo, L.; Granozzi, G.; Cattelan, M.; Agnoli, S. Nanoneedles of Mixed Transition Metal Phosphides as Bifunctional Catalysts for Electrocatalytic Water Splitting in Alkaline Media. *Nanomaterials* **2023**, *13*, 683. [[CrossRef](#)] [[PubMed](#)]
25. Ahmed, A.; Seth, S.; Purewal, J.; Wong-Foy, A.G.; Veenstra, M.; Matzger, A.J.; Siegel, D.J. Exceptional Hydrogen Storage Achieved by Screening Nearly Half a Million Metal–Organic Frameworks. *Nat. Commun.* **2019**, *10*, 1568. [[CrossRef](#)] [[PubMed](#)]
26. Jin, S. How to Effectively Utilize MOFs for Electrocatalysis. *ACS Energy Lett.* **2019**, *4*, 1443–1445. [[CrossRef](#)]
27. Tang, P.; Paganelli, S.; Carraro, F.; Blanco, M.; Riccò, R.; Marega, C.; Badocco, D.; Pastore, P.; Doonan, C.J.; Agnoli, S. Postsynthetic Metalated MOFs as Atomically Dispersed Catalysts for Hydroformylation Reactions. *ACS Appl. Mater. Interfaces* **2020**, *12*, 54798–54805. [[CrossRef](#)] [[PubMed](#)]
28. Liu, X.; Liu, W.; Ko, M.; Park, M.; Kim, M.G.; Oh, P.; Chae, S.; Park, S.; Casimir, A.; Wu, G.; et al. Metal (Ni, Co)–Metal Oxides/Graphene Nanocomposites as Multifunctional Electrocatalysts. *Adv. Funct. Mater.* **2015**, *25*, 5799–5808. [[CrossRef](#)]
29. Xu, X.; Sun, H.; Jiang, S.P.; Shao, Z. Modulating Metal–Organic Frameworks for Catalyzing Acidic Oxygen Evolution for Proton Exchange Membrane Water Electrolysis. *SusMat* **2021**, *1*, 460–481. [[CrossRef](#)]
30. Horcajada, P.; Salles, F.; Wuttke, S.; Devic, T.; Heurtaux, D.; Maurin, G.; Vimont, A.; Daturi, M.; David, O.; Magnier, E.; et al. How Linker’s Modification Controls Swelling Properties of Highly Flexible Iron(III) Dicarboxylates MIL-88. *J. Am. Chem. Soc.* **2011**, *133*, 17839–17847. [[CrossRef](#)]
31. Dan-Hardi, M.; Chevreau, H.; Devic, T.; Horcajada, P.; Maurin, G.; Férey, G.; Popov, D.; Riekkel, C.; Wuttke, S.; Lavalley, J.-C.; et al. How Interpenetration Ensures Rigidity and Permanent Porosity in a Highly Flexible Hybrid Solid. *Chem. Mater.* **2012**, *24*, 2486–2492. [[CrossRef](#)]
32. Yang, S.; Li, X.; Zeng, G.; Cheng, M.; Huang, D.; Liu, Y.; Zhou, C.; Xiong, W.; Yang, Y.; Wang, W.; et al. Materials Institute Lavoisier (MIL) Based Materials for Photocatalytic Applications. *Coord. Chem. Rev.* **2021**, *438*, 213874. [[CrossRef](#)]
33. Taffa, D.H.; Balkenhohl, D.; Amiri, M.; Wark, M. Minireview: Ni–Fe and Ni–Co Metal–Organic Frameworks for Electrocatalytic Water-Splitting Reactions. *Small Struct.* **2022**, *4*, 263. [[CrossRef](#)]
34. Sun, F.; Wang, G.; Ding, Y.; Wang, C.; Yuan, B.; Lin, Y. NiFe-Based Metal–Organic Framework Nanosheets Directly Supported on Nickel Foam Acting as Robust Electrodes for Electrochemical Oxygen Evolution Reaction. *Adv. Energy Mater.* **2018**, *8*, 584. [[CrossRef](#)]
35. Li, F.; Shao, Q.; Huang, X.; Lang, J. Nanoscale Trimetallic Metal–Organic Frameworks Enable Efficient Oxygen Evolution Electrocatalysis. *Angew. Chem. Int. Ed.* **2017**, *57*, 1888–1892. [[CrossRef](#)] [[PubMed](#)]
36. Jia, G.; Zhang, W.; Jin, Z.; An, W.; Gao, Y.; Zhang, X.; Liu, J. Electrocatalytically Active MOF/Graphite Oxide Hybrid for Electrosynthesis of Dimethyl Carbonate. *Electrochim. Acta* **2014**, *144*, 1–6. [[CrossRef](#)]
37. Wu, Y.; Luo, H.; Wang, H. Synthesis of Iron(III)-Based Metal–Organic Framework/Graphene Oxide Composites with Increased Photocatalytic Performance for Dye Degradation. *RSC Adv.* **2014**, *4*, 40435–40438. [[CrossRef](#)]
38. Lalitha, A.; Shin, J.E.; Bonakala, S.; Oh, J.Y.; Park, H.B.; Maurin, G. Unraveling the Enhancement of the Interfacial Compatibility between Metal–Organic Framework and Functionalized Graphene Oxide. *J. Phys. Chem. C* **2019**, *123*, 4984–4993. [[CrossRef](#)]
39. Favaro, M.; Agnoli, S.; Cattelan, M.; Moretto, A.; Durante, C.; Leonardi, S.; Kunze-Liebhäuser, J.; Schneider, O.; Gennaro, A.; Granozzi, G. Shaping Graphene Oxide by Electrochemistry: From Foams to Self-Assembled Molecular Materials. *Carbon* **2014**, *77*, 405–415. [[CrossRef](#)]
40. Mosconi, D.; Kosmala, T.; Lunardon, M.; Neyman, A.; Bar-Sadan, M.; Agnoli, S.; Granozzi, G. One-Pot Synthesis of MoS₂(1–x)Se_{2x} on N-Doped Reduced Graphene Oxide: Tailoring Chemical and Structural Properties for Photoenhanced Hydrogen Evolution Reaction. *Nanoscale Adv.* **2020**, *2*, 4830–4840. [[CrossRef](#)]
41. Favaro, M.; Carraro, F.; Cattelan, M.; Colazzo, L.; Durante, C.; Sambì, M.; Gennaro, A.; Agnoli, S.; Granozzi, G. Multiple Doping of Graphene Oxide Foams and Quantum Dots: New Switchable Systems for Oxygen Reduction and Water Remediation. *J. Mater. Chem. A* **2015**, *3*, 14334–14347. [[CrossRef](#)]
42. Carraro, F.; Cattelan, M.; Favaro, M.; Calvillo, L. Aerosol Synthesis of N and N-S Doped and Crumpled Graphene Nanostructures. *Nanomaterials* **2018**, *8*, 406. [[CrossRef](#)]
43. Lunardon, M.; Ran, J.; Mosconi, D.; Marega, C.; Wang, Z.; Xia, H.; Agnoli, S.; Granozzi, G. Hybrid Transition Metal Dichalcogenide/Graphene Microspheres for Hydrogen Evolution Reaction. *Nanomaterials* **2020**, *10*, 2376. [[CrossRef](#)]
44. Lyu, S.; Guo, C.; Wang, J.; Li, Z.; Yang, B.; Lei, L.; Wang, L.; Xiao, J.; Zhang, T.; Hou, Y. Exceptional Catalytic Activity of Oxygen Evolution Reaction via Two-Dimensional Graphene Multilayer Confined Metal–Organic Frameworks. *Nat. Commun.* **2022**, *13*, 6171. [[CrossRef](#)] [[PubMed](#)]
45. Jayaramulu, K.; Mukherjee, S.; Morales, D.M.; Dubal, D.P.; Nanjundan, A.K.; Schneemann, A.; Masa, J.; Kment, S.; Schuhmann, W.; Otyepka, M.; et al. Graphene-Based Metal–Organic Framework Hybrids for Applications in Catalysis, Environmental, and Energy Technologies. *Chem. Rev.* **2022**, *122*, 17241–17338. [[CrossRef](#)] [[PubMed](#)]
46. Pasarakonda, S.L.; Ponnada, S.; Gorle, D.B.; Chandra Bose, R.S.; Palariya, A.; Kiai, M.S.; Gandham, H.B.; Kathiresan, M.; Sharma, R.K.; Nowduri, A. On the Role of Graphene Oxide in Bifunctional Ni/MOF/RGO Composites in Electrochemical Nitrate Detection and Oxygen Evolution Reaction. *New J. Chem.* **2023**, *47*, 725–736. [[CrossRef](#)]
47. Jahan, M.; Bao, Q.; Loh, K.P. Electrocatalytically Active Graphene–Porphyrin MOF Composite for Oxygen Reduction Reaction. *J. Am. Chem. Soc.* **2012**, *134*, 6707–6713. [[CrossRef](#)] [[PubMed](#)]

48. Mahmood, A.; Yu, Q.; Luo, Y.; Zhang, Z.; Zhang, C.; Qiu, L.; Liu, B. Controllable Structure Reconstruction of Nickel–Iron Compounds toward Highly Efficient Oxygen Evolution. *Nanoscale* **2020**, *12*, 10751–10759. [[CrossRef](#)]
49. Trotochaud, L.; Young, S.L.; Ranney, J.K.; Boettcher, S.W. Nickel–Iron Oxyhydroxide Oxygen–Evolution Electrocatalysts: The Role of Intentional and Incidental Iron Incorporation. *J. Am. Chem. Soc.* **2014**, *136*, 6744–6753. [[CrossRef](#)]
50. Anantharaj, S.; Kundu, S.; Noda, S. “The Fe Effect”: A Review Unveiling the Critical Roles of Fe in Enhancing OER Activity of Ni and Co Based Catalysts. *Nano Energy* **2021**, *80*, 105514. [[CrossRef](#)]
51. Tsuruoka, T.; Furukawa, S.; Takashima, Y.; Yoshida, K.; Isoda, S.; Kitagawa, S. Nanoporous Nanorods Fabricated by Coordination Modulation and Oriented Attachment Growth. *Angew. Chem. Int. Ed.* **2009**, *48*, 4739–4743. [[CrossRef](#)] [[PubMed](#)]
52. Diring, S.; Furukawa, S.; Takashima, Y.; Tsuruoka, T.; Kitagawa, S. Controlled Multiscale Synthesis of Porous Coordination Polymer in Nano/Micro Regimes. *Chem. Mater.* **2010**, *22*, 4531–4538. [[CrossRef](#)]
53. Bagherzadeh, E.; Zebarjad, S.M.; Hosseini, H.R.M. Morphology Modification of the Iron Fumarate MIL-88A Metal–Organic Framework Using Formic Acid and Acetic Acid as Modulators. *Eur. J. Inorg. Chem.* **2018**, *2018*, 1909–1915. [[CrossRef](#)]
54. Bara, D.; Wilson, C.; Mörtel, M.; Khusniyarov, M.M.; Ling, S.; Slater, B.; Sproules, S.; Forgan, R.S. Kinetic Control of Interpenetration in Fe–Biphenyl-4,4′-Dicarboxylate Metal–Organic Frameworks by Coordination and Oxidation Modulation. *J. Am. Chem. Soc.* **2019**, *141*, 8346–8357. [[CrossRef](#)] [[PubMed](#)]
55. Wang, K.; Hui, K.N.; San Hui, K.; Peng, S.; Xu, Y. Recent Progress in Metal–Organic Framework/Graphene-Derived Materials for Energy Storage and Conversion: Design, Preparation, and Application. *Chem. Sci.* **2021**, *12*, 5737–5766. [[CrossRef](#)] [[PubMed](#)]
56. Ferrari, A.C.; Robertson, J. Interpretation of Raman Spectra of Disordered and Amorphous Carbon. *Phys. Rev. B* **2000**, *61*, 14095–14107. [[CrossRef](#)]
57. Hall, D.S.; Lockwood, D.J.; Bock, C.; MacDougall, B.R. Nickel Hydroxides and Related Materials: A Review of Their Structures, Synthesis and Properties. *Proc. Math. Phys. Eng. Sci.* **2015**, *471*, 20140792. [[CrossRef](#)] [[PubMed](#)]
58. Gong, M.; Dai, H. A Mini Review of NiFe-Based Materials as Highly Active Oxygen Evolution Reaction Electrocatalysts. *Nano Res.* **2014**, *8*, 23–39. [[CrossRef](#)]
59. Zhao, S.; Yang, Y.; Tang, Z. Insight into Structural Evolution, Active Sites, and Stability of Heterogeneous Electrocatalysts. *Angew. Chem. Int. Ed.* **2022**, *61*, e202110186. [[CrossRef](#)]
60. Yuan, S.; Peng, J.; Cai, B.; Huang, Z.; Garcia-Esparza, A.T.; Sokaras, D.; Zhang, Y.; Giordano, L.; Akkiraju, K.; Zhu, Y.G.; et al. Tunable Metal Hydroxide–Organic Frameworks for Catalysing Oxygen Evolution. *Nat. Mater.* **2022**, *21*, 673–680. [[CrossRef](#)]
61. Lionet, Z.; Nishijima, S.; Kim, T.-H.; Horiuchi, Y.; Lee, S.W.; Matsuoka, M.; Persidis, A. Bimetallic MOF-Templated Synthesis of Alloy Nanoparticle-Embedded Porous Carbons for Oxygen Evolution and Reduction Reactions. *Nature* **1999**, *17*, 229. [[CrossRef](#)]
62. Cai, Z.; Zhou, D.; Wang, M.; Bak, S.; Wu, Y.; Wu, Z.; Tian, Y.; Xiong, X.; Li, Y.; Liu, W.; et al. Introducing Fe²⁺ into Nickel–Iron Layered Double Hydroxide: Local Structure Modulated Water Oxidation Activity. *Angew. Chem.* **2018**, *130*, 9536–9540. [[CrossRef](#)]
63. Li, P.; Duan, X.; Kuang, Y.; Li, Y.; Zhang, G.; Liu, W.; Sun, X. Tuning Electronic Structure of NiFe Layered Double Hydroxides with Vanadium Doping toward High Efficient Electrocatalytic Water Oxidation. *Adv. Energy Mater.* **2018**, *8*, 3341. [[CrossRef](#)]
64. Wang, Y.; Qiao, M.; Li, Y.; Wang, S. Tuning Surface Electronic Configuration of NiFe LDHs Nanosheets by Introducing Cation Vacancies (Fe or Ni) as Highly Efficient Electrocatalysts for Oxygen Evolution Reaction. *Small* **2018**, *14*, 1800136. [[CrossRef](#)]
65. Zhou, D.; Xiong, X.; Cai, Z.; Han, N.; Jia, Y.; Xie, Q.; Duan, X.; Xie, T.; Zheng, X.; Sun, X.; et al. Flame-Engraved Nickel–Iron Layered Double Hydroxide Nanosheets for Boosting Oxygen Evolution Reactivity. *Small Methods* **2018**, *2*, 83. [[CrossRef](#)]
66. Fang, X.; Jiao, L.; Zhang, R.; Jiang, H.-L. Porphyrinic Metal–Organic Framework-Templated Fe–Ni–P/Reduced Graphene Oxide for Efficient Electrocatalytic Oxygen Evolution. *ACS Appl. Mater. Interfaces* **2017**, *9*, 23852–23858. [[CrossRef](#)]
67. Wang, M.; Lin, M.; Li, J.; Huang, L.; Zhuang, Z.; Lin, C.; Zhou, L.; Mai, L. Metal–Organic Framework Derived Carbon-Confined Ni₂P Nanocrystals Supported on Graphene for an Efficient Oxygen Evolution Reaction. *Chem. Commun.* **2017**, *53*, 8372–8375. [[CrossRef](#)]
68. Jayaramulu, K.; Masa, J.; Tomanec, O.; Peeters, D.; Ranc, V.; Schneemann, A.; Zboril, R.; Schuhmann, W.; Fischer, R.A. Nanoporous Nitrogen-Doped Graphene Oxide/Nickel Sulfide Composite Sheets Derived from a Metal–Organic Framework as an Efficient Electrocatalyst for Hydrogen and Oxygen Evolution. *Adv. Funct. Mater.* **2017**, *27*, 451. [[CrossRef](#)]
69. Ai, L.; Tian, T.; Jiang, J. Ultrathin Graphene Layers Encapsulating Nickel Nanoparticles Derived Metal–Organic Frameworks for Highly Efficient Electrocatalytic Hydrogen and Oxygen Evolution Reactions. *ACS Sustain. Chem. Eng.* **2017**, *5*, 4771–4777. [[CrossRef](#)]
70. Jiao, L.; Zhou, Y.-X.; Jiang, H.-L. Chemical Science Metal–Organic Framework-Based CoP/Reduced Graphene Oxide: High-Performance Bifunctional Electrocatalyst for Overall Water Splitting Metal–Organic Framework-Based CoP/Reduced Graphene Oxide: High-Performance Bifunctional Electrocatalyst for Overall Water Splitting. *Chem. Sci.* **2016**, *7*, 1615–2442. [[CrossRef](#)]

Disclaimer/Publisher’s Note: The statements, opinions and data contained in all publications are solely those of the individual author(s) and contributor(s) and not of MDPI and/or the editor(s). MDPI and/or the editor(s) disclaim responsibility for any injury to people or property resulting from any ideas, methods, instructions or products referred to in the content.